A sensitive time-resolved radiation pyrometer for shock-temperature measurements above 1500 K

Mark B. Boslough

Sandia National Laboratories, Albuquerque, New Mexico 87185

Thomas J. Ahrens

Seismological Laboratory, California Institute of Technology, Pasadena, California 91125

(Received 31 March 1989; accepted for publication 7 August 1989)

An optical system has been developed which can determine time-resolved temperatures in shocked materials by measuring the spectral radiance of light emitted from shocked solid samples in the visible and near-infrared wavelength range (0.5–1.0 μm). It can measure temperatures as low as 1500 K and has been successfully used to observe shock-induced chemical reactions in powder samples. The high sensitivity of this radiation pyrometer can be attributed to the large angular aperture (0.06 sr), the large bandwidth per channel (up to 0.1 μm), the large photodiode detection areas (1.0 cm^2), and the small number of calibrated channels (4) among which light is divided. Improved calibration techniques, as well as the layout of the instrument, eliminate certain sources of error encountered in previous shock-temperature experiments. Errors in the measured spectral radiance were reduced by: (1) recalibration before every experiment to account for changes in optical components; (2) direct calibration of voltage recorded at each digitizer to prevent transfer error by an intermediate step; (3) use of a spectral irradiance calibration lamp to exclude errors due to spatial inhomogeneities associated with spectral radiance sources; and (4) obtaining a large spatial average of light at each wavelength from the same portion of the sample to eliminate errors from possible inhomogeneities in the sample. The magnitude each of these errors could previously contribute was 1%–2% of the total signal. Absolute temperature uncertainties, determined from the standard deviation of the measured spectral radiances from the least-squares-fit values, are typically about 5%. Emissivities are poorly constrained by spectral radiance data because of a weak functional dependence, and uncertainties can easily exceed 50% for temperatures of around 2000 K.

INTRODUCTION

Time-resolved radiation pyrometry has proven to be a useful tool in the study of condensed matter in the shocked state. It has been applied to problems in condensed matter physics and chemistry, high explosives, and high-pressure geophysics. In many ways it complements other optical experimental methods such as spectroscopy and high speed framing and streak photography. Not only can shock temperatures be measured but, in some cases, the optical properties of the shocked state can be determined from the time dependence of the radiated light.[1] The method has been used to constrain high pressure equations of state, detect and quantify phase transformations, and study shock-induced chemical reactions.

The first application of pyrometry to study shocked materials was by Kormer *et al.*,[2,3] who measured light emitted from initially transparent solids at two different wavelengths and were able to determine color temperatures. Subsequently, various types of pyrometers have been used by Raikes and Ahrens[4] to measure residual temperatures of shocked minerals, by Von Holle[5] in studies of reacting high explosives, by Lyzenga and others[6–9] and Ahrens *et al.*[10] to determine high pressure thermal equations of state, and by Radousky and co-workers[11,12] for studies of shocked fluids. A similar device has been used by Brannon *et al.*[13] to measure shock-induced nonthermal light radiated from solids.

The present system was designed to be more sensitive to spectral radiance (and therefore to lower temperatures) than previous pyrometers, while at the same time providing a high degree of precision and time resolution. High sensitivity was achieved in part by increasing the spectral bandwidths and photodetector area beyond what had previously been used. The corresponding reductions in spectral resolution and time response did not significantly reduce the quality of the data.

The generic design of the present pyrometer was initially implemented by Boslough[14] on the Caltech two-stage light-gas gun,[15] which launches 25 mm diam projectiles that strike specimens at speeds of 4–7 km/s. Shock pressures in the 50–200 GPa range are generated during the propagation time of the shock wave through the sample. This original instrument has been applied mostly to problems in high pressure geophysics (e.g., Boslough *et al.*[16]) and was used in conjunction with other techniques by Williams *et al.*[17] to estimate the temperature of the Earth's core. A more sensitive system, which is described in the present article, was designed to be used with Sandia's 25-m single-stage gas-gun,[18] which launches 63 mm diam projectiles at speeds up to 1.2 km/s and achieves shock pressures up to 25 GPa in

 0034-6748/89/123711-06$01.30

samples of interest. This newer pyrometer has been used primarily for studies of shock-induced chemical reactions in powders.[19]

I. EXPERIMENT DESIGN

The description of the newer radiation pyrometer (Fig. 1) will proceed in the direction of light propagation, beginning with the target assembly. A number of types of targets have been used. Of current interest are measurements of light radiated from shocked powders. These experiments are performed in one of two ways. One method makes use of a target consisting of a transparent solid, usually lithium fluoride, which is struck directly by an impactor containing a powder pellet carried on the face of a projectile. In these "reverse impact" experiments, the initial shock state in the pellet is viewed by the pyrometer. The other type of target consists of a powder pellet with an attached transparent window (or anvil), again usually lithium fluoride. In these "direct impact" experiments, the first state observed by the pyrometer is actually the second (reflected) shock state. A version of this target is depicted in Fig. 2. In either case, two coaxial shorting pins are mounted on either side of the sample to provide triggering pulses before impact.

To observe a single, well-defined state the sample edge must be masked, because the field of view of the pyrometer is greater than the portion of the sample in which one-dimensional wave motion occurs during times of interest. Edge effects (two-dimensional flow) occur at only the outer edges of the sample. For this reason an aluminum edge-mask (anodized black) is attached to the free surface of the transparent window. The mask contains a central hole which provides the only path for light from the sample to enter the pyrometer. A large set of experiments[20] has demonstrated that, for a properly designed target, there are no other sources of light which can contaminate the signal, a problem that had been experienced previously.[21]

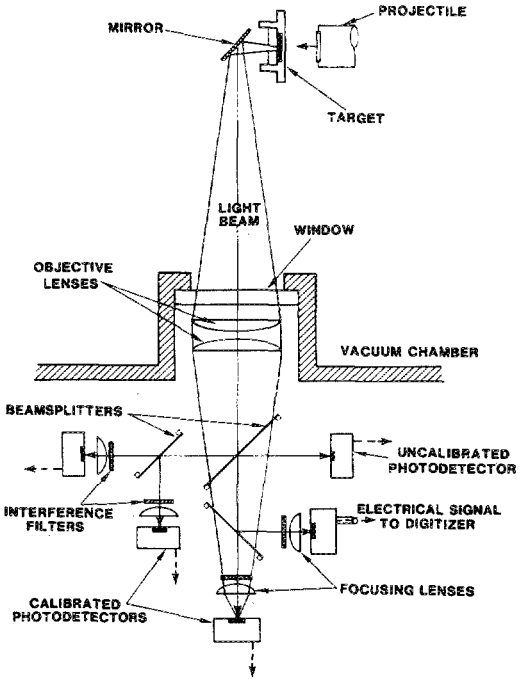

FIG. 1. Schematic diagram of radiation pyrometer, showing its relation to gas-gun impact chamber.

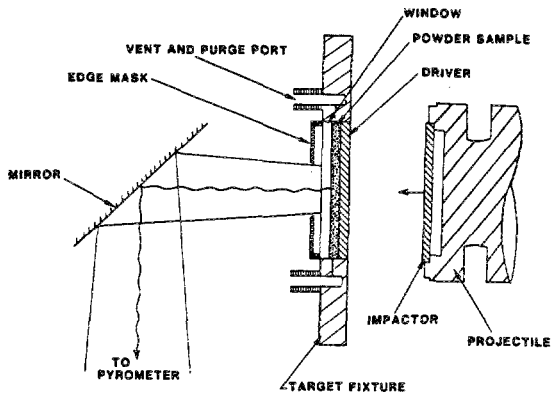

FIG. 2. An example of a powder target assembly. This configuration was designed for direct impact experiments.

The circular aperture varies in diameter from 6 to 25 mm depending on the particular target design. The light radiated by the sample is reflected by an aluminized mirror, turning it toward the radiation pyrometer port in the target chamber. This port is covered with a protective Pyrex window that separates the target chamber from the objective lenses, which are two crown glass plano-convex lenses, with focal lengths of 50 cm and clear apertures of 14 cm. The target is near the focal point of the first lens. The collected light is separated into four legs by three reflective-coated pellicle beamsplitters. Each of the four resulting beams falls upon a detector assembly, which consists of an interference filter, a focusing lens, and a photodiode with a bias circuit. The bandpass filters are 50 mm in diameter and have peak wavelengths in the visible or near-infrared within the effective bandwidth range of the silicon photodiodes. The filters have half-height bandwidths of 0.1 μm or less.

The detectors used were RCA C30810 *N*-type silicon pin photodiodes, with an active area of 1.0 cm^2. Germanium photodiodes have also been used to extend the wavelength range further into the infrared, but the poorer frequency response of germanium complicates the data reduction. To ensure that the image of the sample (and calibration lamp filament) falls entirely within the photodiode active area, a 52-mm-diameter, 32-mm focal length aspheric glass focusing lens is positioned between the filter and photodiode. This demagnifies the image by a factor of about 0.3. The detector assemblies are mounted on three-axis translation stages to allow for alignment and focus adjustments. The focusing lens and filter holder can be moved independently to permit separate adjustment of focus and demagnification.

This optical configuration ensures that each detector views precisely the same area of the target. Thus, when radiation is heterogeneously emitted, as is the case when shear bands or hot spots develop (e.g., Kondo and Ahrens[22]), the average brightness is measured by each detector. This eliminates the possibility of an erroneous temperature measurement due to different detectors viewing different target areas

which may not have the same temperature distribution. Also, by viewing the entire unmasked portion of the target, the sensitivity of the instrument is increased. Because the image is demagnified there is sufficient tolerance in alignment and focusing, as long as the entire image falls within the active area of the detector.

The silicon photodiode circuit supplies a 45 V reverse bias from a dc power supply to the photodiode. Signals are transmitted by terminated 50-Ω cables, and recorded by an array of LeCroy 6880 and Tektronix 7612 digitizers. There is also an optional unfiltered, uncalibrated fifth channel which consists of an RCA C30872 silicon avalanche photodiode. It has a nominal rise time of 2 ns, and provides fast time response to ensure that any high-frequency component of the light is recorded. This photodiode is positioned where it receives stray light reflected from one of the optical filters. Its output can be recorded by a high frequency digital oscilloscope, but is not used in the temperature calculation.

II. CALIBRATION PROCEDURE

Unlike previous shock pyrometers which used a spectral radiance source for calibration, the present system uses a spectral irradiance source. A spectral radiance source typically consists of a tungsten ribbon which can have a nonuniform temperature distribution over its surface. During calibration the possibility exists that different photodetectors measure light from different parts of the ribbon, leading to calibration error. By contrast, a spectral irradiance source is usually a tungsten filament. During calibration, the image of the entire source filament falls entirely within the active area of each photodetector. All detectors therefore view exactly the same light source, thereby reducing the calibration error.

The standard of spectral irradiance is placed in the position of the target in the impact chamber and the pyrometer is aligned. The spectral irradiance is given in units of $\mu W/cm^2$ nm at a distance of 50 cm (a surface 50 cm from the lamp receives the given spectral irradiance). At this distance, 1 cm^2 of area subtends a solid angle of 0.0004 sr, so the spectral radiant intensity (power per unit solid angle per unit wavelength) of the lamp is equal to its spectral irradiance divided by 0.0004 sr/cm.[2] Since the entire lamp filament is imaged onto the photodiodes, its spectral radiant intensity is equivalent to that of a point source. The standard source used is a commercial General Electric type Q6.6A/T4Q/5CL 200 W tungsten coil filament quartz-halogen lamp calibrated by Optronics Laboratories, Inc. by transfer from a National Bureau of Standards source. Use of this lamp as a standard is described by Schneider and Goebel.[23] The lamp is mounted on a target assembly and aligned in the same manner as a real target, using the same mirror and window as are used in the actual experiment. It is driven by 6.50 A from an Optronics Laboratories, Inc., model 83DS precision dc constant current power supply. The use of dc current avoids the 120-Hz ripple in light intensity associated with calibration lamps powered by ac current, thereby eliminating another source of error that has been experienced in the past.

For calibration of the pyrometer with the Tektronix 7612 digitizers, the light beam incident on the pyrometer is mechanically chopped at approximately 250 Hz, and the resulting square wave is recorded for each detector. The voltage amplitude of the square wave, as recorded on each channel, is divided into the spectral radiant intensity of the lamp at the mean effective wavelength of its corresponding filter, resulting in a calibration factor. The appropriate spectral irradiance for calibration is found by interpolating between values given by a table supplied by Optronics Laboratories for the quartz halogen lamp. The pyrometer is calibrated with the LeCroy 6880 digitizers similarly, but because of the short sampling window of these digitizers (about 7 μs maximum), the light source cannot be physically chopped fast enough. Instead, a number of measurements are made with the lamp both on and off, and averaged to compensate for baseline drift and other effects normally accounted for by using the mechanical chopper. The resulting calibration factors are multiplied by the amplitude of the experimental waveform to get a time-resolved spectral radiant intensity for the shocked material. To determine the spectral radiance from which the temperature is calculated, spectral radiant intensity is divided by the area of the aperture in the edge mask. The actual solid angle subtended by the objective lens need not be known, as long as the calibration lamp is used in the same position as the target. This procedure is carried out prior to every experiment, to account for differences between the expendable components (the mirror and window), and minor differences in experimental configuration, cleanliness of optics, etc. It is not necessary to carry out a voltage calibration on the recording digitizers because for each channel the same digitizer is used for both calibration and experiment. This procedure takes a potentially error-compounding step out of the calibration process.

Because of the large (up to 0.1 μm) half-height bandwidths of the filters used with this pyrometer, it is necessary to calculate the mean effective wavelength of each filter, which depends on the spectral dependence of the other optical components, and on the temperature of the source. The other optical components have only a weak wavelength dependence relative to the filters, and this does not change greatly from experiment to experiment as components are replaced. It is thus possible to use nominal values published in component specifications, and representative values for the expendable components (the mirror and window) without greatly affecting the results. The wavelength-dependent parameters of the various optical components (Fig. 3) are defined in Table I. All are functions of λ, the wavelength in vacuum.

The spectral reduction factors for each pyrometer station, $r_i(\lambda)$ are given by

$$r_1(\lambda) = R_M T_W T_L^2 T_{B_1} T_{B_2} T_I T_1 R_d, \quad (1)$$

$$r_2(\lambda) = R_M T_W T_L^2 T_{B_1} R_{B_2} T_I T_2 R_d, \quad (2)$$

$$r_3(\lambda) = R_M T_W T_L^2 R_{B_1} R_{B_2} T_I T_3 R_d, \quad (3)$$

$$r_4(\lambda) = R_M T_W T_L^2 R_{B_1} T_{B_2} T_I T_4 R_d. \quad (4)$$

These factors are multiplied by T_p, the transmittance of the anvil, for every experiment except those in which light is measured directly from the free surface of the target.

The mean wavelength of channel i is therefore

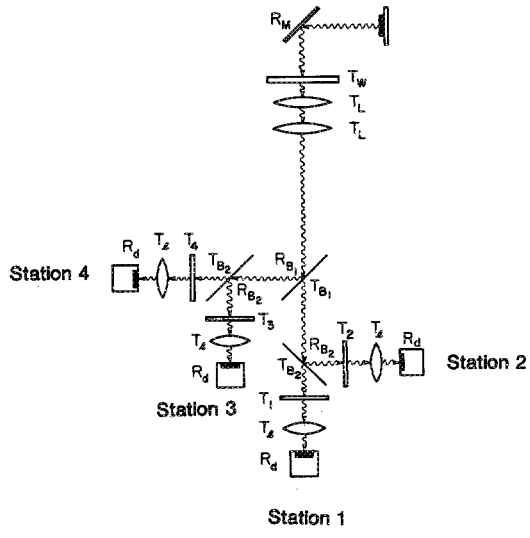

FIG. 3. Expanded diagram of radiation pyrometer. Components are labeled with symbols defined in Table I.

$$\bar{\lambda}_i = \left(\int_0^\infty r_i(\lambda)\lambda\, d\lambda\right) \Big/ \left(\int_0^\infty r_i(\lambda) d\lambda\right). \tag{5}$$

There will also be a shift in effective wavelength as a function of temperature of the source, and this should be included. To calculate the shift, we must assume *a priori* that the source radiates with a spectral distribution described by the Planck function. In most of the experiments to date, the results indicate that this assumption is indeed valid.

The mean effective wavelength $\hat{\lambda}_i(T)$ is defined to be the temperature dependent wavelength such that

$$f[T,\hat{\lambda}_i(T)] = \frac{\int_0^\infty r_i(\lambda) f(T,\lambda) d\lambda}{\int_0^\infty r_i(\lambda) d\lambda}, \tag{6}$$

where $f(T,\lambda)$ is the Planck function

$$f(T,\lambda) \sim \lambda^{-5}[\exp(hc/k_b\lambda T) - 1]^{-1}, \tag{7}$$

and h, c, and k_b are Planck's constant, the speed of light and Boltzman's constant, respectively. $\hat{\lambda}_i(T)$ can be found by numerically evaluating Eq. (6). The mean effective wavelengths are weak functions of temperature for the pyrometer station-filter combinations which have been used to date, except at temperatures for which Wien's Law places the maximum of the Planck function near the mean wavelength of the filter. Two examples are plotted in Fig. 4.

TABLE I. Definitions of optical parameters.

Parameter	Definition
R_M	Reflectance of turning mirror
T_W	Transmittance of glass window
T_L	Transmittance of objective lens
T_{B_1}	Transmittance of primary beamsplitter
R_{B_1}	Reflectance of primary beamsplitter
T_{B_2}	Transmittance of secondary beamsplitter
R_{B_2}	Reflectance of secondary beamsplitter
T_l	Transmittance of focusing lens
$T_{1,2,3,4}$	Transmittance of optical bandpass filters
R_d	Responsivity of photodetector

III. TEMPERATURE DETERMINATION

Once the values of spectral radiance N_λ are determined at each of the four wavelengths, a two-parameter least-squares (graybody) calculation can be carried out to find the temperature T and effective emissivity ϵ. It is important to note here that in general there is not a single temperature associated with the shocked material, but a range of temperatures, as in the case of hot spots, shear band heating, or inhomogeneous chemical reaction. Because spectral radiance is such a strong function of temperature, the least-squares method is highly skewed in favor of the highest temperature present. Depending on the true temperature distribution, this temperature calculation may or may not give a precise measure of the highest temperature present in the sample. For example, a bimodal temperature distribution, in which the high temperature region is much hotter than the rest of the sample, will give rise to a precise measurement, whereas a broad temperature distribution (many temperatures present) may not. The precision of the measurement can be found by the quality of the fit of the graybody distribution function to the data.

The graybody distribution function is the Planck function [Eq. (7)] which can be written in the form

$$N_\lambda = \epsilon C_1 \lambda^{-5}(e^{C_2/\lambda T} - 1)^{-1}, \tag{8}$$

where C_1 and C_2 are constants equal to 1.191×10^{-16} and 1.439×10^{-2}, respectively, in mks units. The effective emissivity is $\epsilon = \epsilon_0\alpha$, where ϵ_0 is the actual emissivity of the radiating material, and α is the fraction of the observed area that is radiating light. To carry out the least-squares fit, we make initial guesses for temperature (T^0) and effective emissivity (ϵ^0) and determine the calculated spectral radiance (N_λ^0) from Eq. (8). We compute $\Delta T = T - T^0$ and $\Delta\epsilon = \epsilon - \epsilon^0$ from the equation

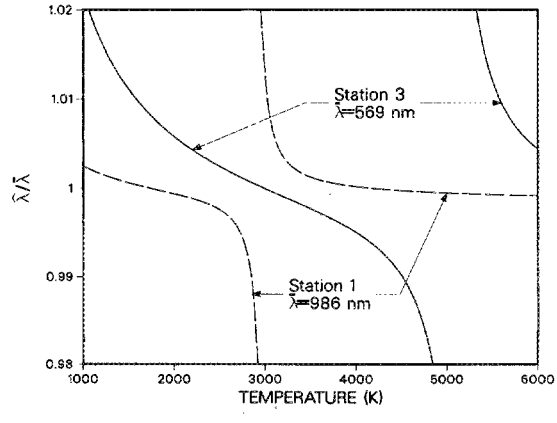

FIG. 4. Mean effective wavelength $\hat{\lambda}$, as defined by Eq. (6), of two pyrometer station-filter combinations, normalized to filter mean wavelength $\bar{\lambda}$. The mean effective wavelength is the wavelength a bandpass filter would have to have in the limit of zero bandwidth in order to pass the same amount of light from a Planck source as the actual filter. At temperatures away from those at which the filter wavelength is at the Wien's Law maximum, the corrections are small. At the maximum, the corrections are large but unnecessary.

$$N_\lambda - N_\lambda^0 = \frac{\partial N_\lambda}{\partial T}\Delta T + \frac{\partial N_\lambda}{\partial \epsilon}\Delta\epsilon. \quad (9)$$

It is a simple matter to determine the partial derivatives analytically from Eq. (8). By using ΔT and $\Delta\epsilon$ to obtain new trial values for T and ϵ, we can iterate until convergence is reached. In order to get time-resolved temperatures, this entire procedure is carried out for each time step. It is useful to use the final values for T and ϵ at a given time step for the initial guesses for the following step, as these parameters are generally smooth functions of time.

It is important to recall here that the mean effective wavelengths of the pyrometer channels are functions of temperature (Fig. 4), due to the large bandwidths. Carrying out the least-squares procedure as outlined above, using fixed wavelengths, is not sufficient to get the best answer. The effective pyrometer wavelengths can be recalculated based on the temperature being measured. This process can be carried out iteratively, and tends to converge rapidly, giving rise to a minor correction. In practice, for the filter bandwidths we have used, this correction is smaller than the temperature uncertainty, and is therefore unnecessary.

Uncertainties in temperature and emissivity were determined systematically by the equations

$$\delta T = \sigma_N \Big/ \left(\frac{\partial N_\lambda}{\partial T}\right)_{\epsilon,\lambda=\langle\lambda\rangle}, \quad (10)$$

$$\delta\epsilon = \sigma_N \Big/ \left(\frac{\partial N_\lambda}{\partial \epsilon}\right)_{T,\lambda=\langle\lambda\rangle}, \quad (11)$$

where σ_N is the standard deviation in spectral radiance, and the partial derivatives are evaluated at $\langle\lambda\rangle$, i.e., the average wavelength of all the pyrometer channels.

IV. RESULTS AND DISCUSSION

The present system has been used primarily to measure light emission from inert and reactive powder mixtures. Time-resolved spectral radiance data from one experiment are shown in Fig. 5. The target consisted of a thin (about 0.5 mm) powder layer sandwiched between a copper driver plate and a lithium fluoride window, similar to Fig. 2. In this experiment, the powder was a mixture of 2-μm particle-size nickel and 1-μm particle-size aluminum in a 87%/13% ratio by weight, with an initial porosity of 57%. Shock-recovery[24] experiments have shown that this composition chemically reacts under shock. The target was struck by a copper impactor traveling at 1.18 km/s, achieving a peak shock pressure of about 14 GPa in the powder sample.

The time-resolved temperature and emissivity histories computed by the least-squares method are illustrated in Fig. 6. The measured temperature drops from about 2700 to 2000 K in the first microsecond after shock arrival. The initial high temperature is due to heterogeneous distribution of the shock energy. The total radiant energy is dominated by light emitted from the fraction of the observed area that is hotter that the rest, until thermal equilibrium is established. As thermal equilibrium is achieved, the highest observed temperature rapidly decreases to the mean bulk shock temperature, with an associated increase in effective emissivity as the fractional area of radiating sample increases to unity. At this time, the temperature continues to decrease more slowly by conduction of heat into the lithium fluoride window by a process modelled by Grover and Urtiew.[25] It should also be noted that the double peak at early times is due to a reflected shock in the thin powder layer.

The quality of the least-squares fit is shown by Fig. 7. The plot shows four measured spectral radiances from the experiment, 1 μs after arrival of the shock wave. The curve represents the best-fitting graybody function, with $T = 2100 \pm 150$ K and $\epsilon = 0.205 \pm 0.128$, where the uncertainties are determined by Eqs. (10) and (11). Emissivities are typically poorly constrained by visible spectral radiance data for temperatures in this range, due to the weak dependence of spectral radiance on emissivity in Eq. (8). However, the strong dependence of spectral radiance on temperature leads to relatively small uncertainties in temperature. In this case the temperature is well enough constrained to conclude that heat has been released from the chemical reaction initiated by the shock wave. The measured shock temperature exceeds the theoretical shock temperature, calculated assuming there is no chemical reaction, by more than 600 K.[26]

Radiation pyrometry is extremely useful in measuring properties of the shock state, but other methods should also

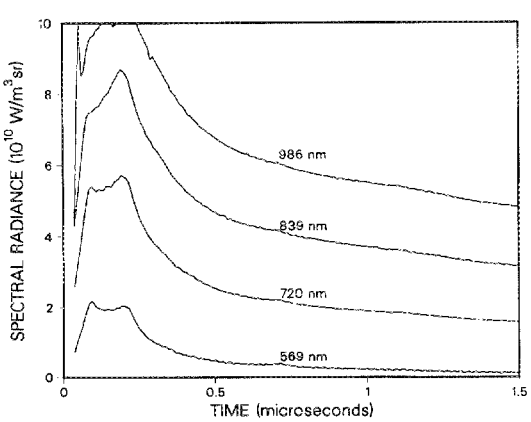

FIG. 5. Time-resolved data from nickel-aluminum powder mixture shocked to about 14 GPa. Origin of time axis corresponds to shock arrival at powder-window interface. Each curve is offset vertically from the curve below it by 10^{10} W/m^3 sr for display purposes. The lowest curve is not offset.

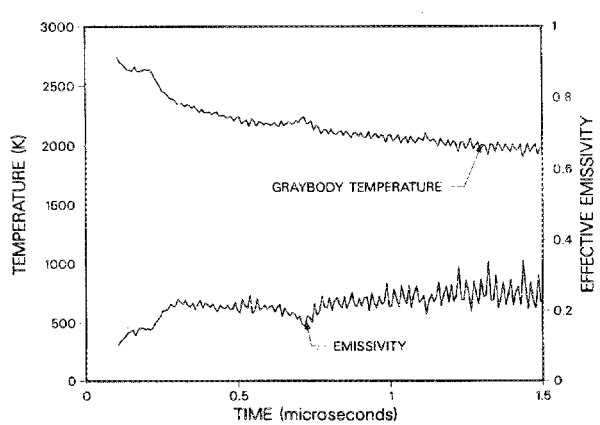

FIG. 6. Time-resolved temperature and emissivity data calculated from spectral radiance data in Fig. 5.

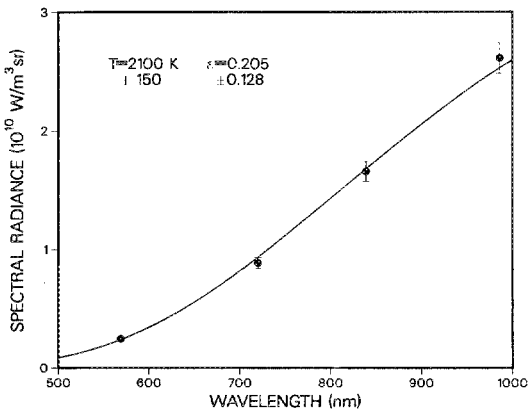

FIG. 7. Spectral radiances from Fig. 5 plotted for the time step $t = 1\,\mu$s, with the best fitting graybody curve corresponding to $T = 2100$ K and $\epsilon = 0.205$.

be employed in order for an experimental program to be more complete. There are three principal variables to deal with when making measurements of shock-induced emission of radiation: wavelength, position, and time. These can be envisioned to define a three-dimensional space. Radiation pyrometry averages over the spatial dimension, obtains data discretely in the spectral dimension and continuously in the temporal dimension. Complimentary methods define "orthogonal" planes in variable space. Fast framing photography provides spatial resolution, discrete temporal information, and no spectral information. Streak photography provides continuous temporal data, spatial resolution in one direction, but again no spectral information. Gated spectroscopy provides the spectral resolution at discrete times, but no spatial resolution. There has been recent work in combining spectroscopy with streak photography,[27] which results in continuous data in the wavelength-time plane; however, it is not possible to get precise values of spectral radiance with this method. It is clear that no single experimental method can obtain a complete picture, and that radiation pyrometry is only one of several complementary experimental techniques which can be employed to study shock-induced light emission.

ACKNOWLEDGMENTS

We are grateful for the advice and assistance of M. Anderson, G. Lyzenga, D. Schmitt, and R. Setchell. This work was performed at Sandia National Laboratories by DOE contract No. DE-ACO4-76DP00789. It was supported at the California Institute of Technology under NASA Grant No. NGL-05-002-105 and NSF Grant No. EAR86-08249, Contribution No. 4073, Division of Geological and Planetary Sciences, California Institute of Technology.

[1] M. B. Boslough, J. Appl. Phys. **58**, 3394 (1985).
[2] S. B. Kormer, M. V. Sinitsyn, G. A. Kirillov, and V. D. Urlin, Sov. Phys. JETP **21**, 689 (1965).
[3] S. B. Kormer, Sov. Phys. Usp. Engl. Transl. **11**, 229 (1968).
[4] S. A. Raikes and T. J. Ahrens, Geophys. J. R. Astr. Soc. **58**, 717 (1979).
[5] W. G. Von Holle, *Fast Reactions in Energetic Systems*, edited by C. Capellos and R. F. Walker (Kluwer, Boston 1981), p. 485.
[6] G. A. Lyzenga and T. J. Ahrens, Rev. Sci. Instrum. **50**, 1421 (1979).
[7] G. A. Lyzenga and T. J. Ahrens, Geophys. Res. Lett. **7**, 141 (1980).
[8] G. A. Lyzenga, T. J. Ahrens, and A. C. Mitchell, J. Geophys. Res. **88**, 2431 (1983).
[9] G. A. Lyzenga, T. J. Ahrens, W. J. Nellis, and A. C. Mitchell, J. Chem. Phys. **76**, 6282 (1982).
[10] T. J. Ahrens, G. A. Lyzenga, and A. C. Mitchell, *High-Pressure Research in Geophysics*, edited by S. Akimoto and M. H. Manghnani (Reidel, Boston, 1982), p. 579.
[11] H. B. Radousky, W. J. Nellis, M. Ross, D. C. Hamilton, and A. C. Mitchell, Phys. Rev. Lett. **57**, 2419 (1986).
[12] H. B. Radousky and M. Ross, Phys. Lett. A **129**, 43 (1988).
[13] P. J. Brannon, C. H. Konrad, R. W. Morris, E. D. Jones, and J. R. Asay, J. Appl. Phys. **54**, 6374 (1983).
[14] M. B. Boslough, Ph.D thesis, California Institute of Technology, 1983.
[15] R. Jeanloz and T. J. Ahrens, *High-Pressure Research-Applications in Geophysics*, edited by M. H. Manghnani and S. Akimoto (Academic, New York, 1977), p. 439.
[16] M. B. Boslough, T. J. Ahrens, and A. C. Mitchell, Geophys. J. R. Astr. Soc. **84**, 475 (1986).
[17] Q. Williams, R. Jeanloz, J. Bass, B. Svendsen, and T. J. Ahrens, Science **236**, 181 (1987).
[18] R. E. Setchell, *Shock Waves in Condensed Matter 1981*, edited by W. J. Nellis, L. Seaman, and R. A. Graham (American Institute of Physics, New York, 1982), p. 657.
[19] M. B. Boslough, Int. J. Impact Eng. **5**, 173 (1987).
[20] M. B. Boslough, R. E. Setchell, M. U. Anderson, M. R. Lewis, and D. E. Wackerbarth, Sandia Report SAND88-2768, 1989 (unpublished).
[21] M. Nicol, S. W. Johnson, and N. C. Holmes, *Shock Waves in Condensed Matter 1987*, edited by S. C. Schmidt and N. C. Holmes (North-Holland, Amsterdam, 1988), p. 471.
[22] K. Kondo and T. J. Ahrens, Phys. Chem. Minerals **9**, 173 (1983).
[23] W. E. Schneider and D. G. Goebel, Light Measurement '81, Proc. SPIE **262**, 74 (1981).
[24] Y. Horie, R. A. Graham, and I. K. Simonsen, Mater. Lett. **3**, 354 (1985).
[25] R. Grover and P. A. Urtiew, J. Appl. Phys. **45**, 146 (1974).
[26] M. B. Boslough, Chem. Phys. Lett. **160**, 618 (1989).
[27] R. E. Setchell, AIAA Progress in Astronautics and Aeronautics **106**, 607 (1986).